LUND UNIVERSITY

Versatile multispectral microscope based on light emitting diodes.

Brydegaard, Mikkel; Merdasa, Aboma; Jayaweera, Hiran; Ålebring, Jens; Svanberg, Sune

Link to publication

Versatile multispectral microscope based on light emitting diodes

Mikkel Brydegaard, Aboma Merdasa, Hiran Jayaweera, Jens Ålebring, and Sune Svanberg

Related Articles

Total internal reflection fluorescence microscopy imaging-guided confocal single-molecule fluorescence spectroscopy
Rev. Sci. Instrum. 83, 013110 (2012)

A high accuracy femto-/picosecond laser damage test facility dedicated to the study of optical thin films
Rev. Sci. Instrum. 83, 013109 (2012)

Two-photon focal modulation microscopy in turbid media
Appl. Phys. Lett. 99, 233702 (2011)

A high-reflectivity, ambient-stable graphene mirror for neutral atomic and molecular beams
Appl. Phys. Lett. 99, 211907 (2011)

Sum frequency generation-compressive sensing microscope
J. Chem. Phys. 135, 194202 (2011)

Additional information on Rev. Sci. Instrum.

Versatile multispectral microscope based on light emitting diodes

Mikkel Brydegaard,[1] Aboma Merdasa,[1,2] Hiran Jayaweera,[1,3] Jens Ålebring,[1] and Sune Svanberg[1]

[1]*Division of Atomic Physics, Lund University, SE-221 00 Lund, Sweden*
[2]*ICFO, Institute of Photonic Sciences, Av. del Canal Olímpic, 08860 Barcelona, Spain*
[3]*Department of Physics, University of Colombo, Colombo 03, Sri Lanka*

We describe the development of a novel multispectral microscope, based on light-emitting diodes, capable of acquiring megapixel images in thirteen spectral bands from the ultraviolet to the near infrared. The system captures images and spectra in transmittance, reflectance, and scattering modes. We present as examples of applications ground truth measurements for remote sensing and parasitology diagnostics. The system is a general purpose scientific instrument that could be used to develop dedicated simplified instruments with optimal bands and mode selection. © *2011 American Institute of Physics*. [doi:10.1063/1.3660810]

I. INTRODUCTION

Optical diagnostics involving optical spectroscopy is now applied in a vast range of research fields, including biomedicine, zoology, remote sensing, food sciences, and agriculture (see, e.g., Refs. 1 and 2). The backbone of advanced optical diagnostics involving photon transport usually starts by measuring the basic optical properties of the sample of interest, such as, its reflectance, transmission, absorption, scattering, or fluorescent yields.[3,4] These optical properties of the sample govern the extension of the interrogation volume in a variety samples on largely different scales; e.g., interstellar dust,[5] planetary atmospheres,[6] forest canopies,[7] living tissue,[8] bird plumage,[9] or photon migration within a single grain of rice.[10] Basic optical diagnostics often involves several steady-state measurements with an integrating sphere, e.g., total reflectance, total transmittance, and collimated transmittance.[11] Due to high requirements on radiance, broadband light is usually created with high-pressure xenon-mercury lamps, collimated into fibers, and then directed at the sample. After interaction with a sample of known thickness, the light propagation angle is measured in a number of angular intervals (discretized), representing total reflectance, transmittance, and collimated transmittance, and the light is collected and analyzed with multichannel spectrometers. For highly fluorescent samples, and when studying optical properties in the UV region, even the wavelength of the excitation light source must be selected (discretized) with an additional monochromator to separate reflectance from fluorescence.[12] The optical efficiency (photon economy) is usually poor in these setups, since light is lost every time the beam is divided. The area studied can be rather large, and the samples must be of a considerable size. Since the measurements are averaged spatially over the beam profile, it is impossible to describe the variation of properties within the sample. For example, a hole in the sample would increase the total transmittance in the same way as if the sample had been thinner or more transparent. The advantage of imaging spectroscopy is thus evident.

The stability of the spectrum produced by XeHg lamps is usually poor because of the turbulence caused by the extreme pressure and temperature, which makes calibration unreliable. In addition the relatively long acquisition time introduces uncertainties resulting from sample drying, or photobleaching and photokinetics, which may cause non-linear absorption and fluorescence.[13] A number of alternative methods exist, including time-resolved methods which are able to separate scattering and absorption phenomena,[14,15] and spatially resolved methods, where diffuse reflectance distributions are studied.[16] The acquisition time is usually long, the number of spectral bands is limited, and considerable sample volumes must be used for certain assumptions to be valid.

The recent development of light-emitting diodes (LEDs) as light sources[17] has afforded several advantages, including simplicity, reduced cost, and increasing emission yields every year. Stability has been improved[18] and modulation speed increased to the sub-nanosecond scale.[19,20] The light emitted from these devices currently ranges from 240 nm to 7 μm.[21] Their use in diagnostic instrumentation implies a significant improvement in performance, due to the fact that spectroscopy can be performed in the illumination side, without losses due to wavelength selection, rather than on the detection side using lossy spectrometers or filters. The corresponding technology for acquiring multispectral images sequentially on the detection side would be imaging through costly interference filter wheels or tunable liquid crystal filters.

The recent development of complementary metal–oxide–semiconductor (CMOS) imagers[22] and industrial imagers for inspection provides millions of spatial light measurements. Also, they now include features such as fast triggering, synchronization, extended dynamic ranges, and the interesting feature of having no blooming, an intrinsic feature which allows measurements, even if parts of the image are saturated.

We present a LED-based multispectral microscope, which can be considered as an imaging spectrometer with improved photon economy, and reduced cost, capable of measuring the optical properties of samples with sizes ranging from few micrometers to a millimeter. The instrument
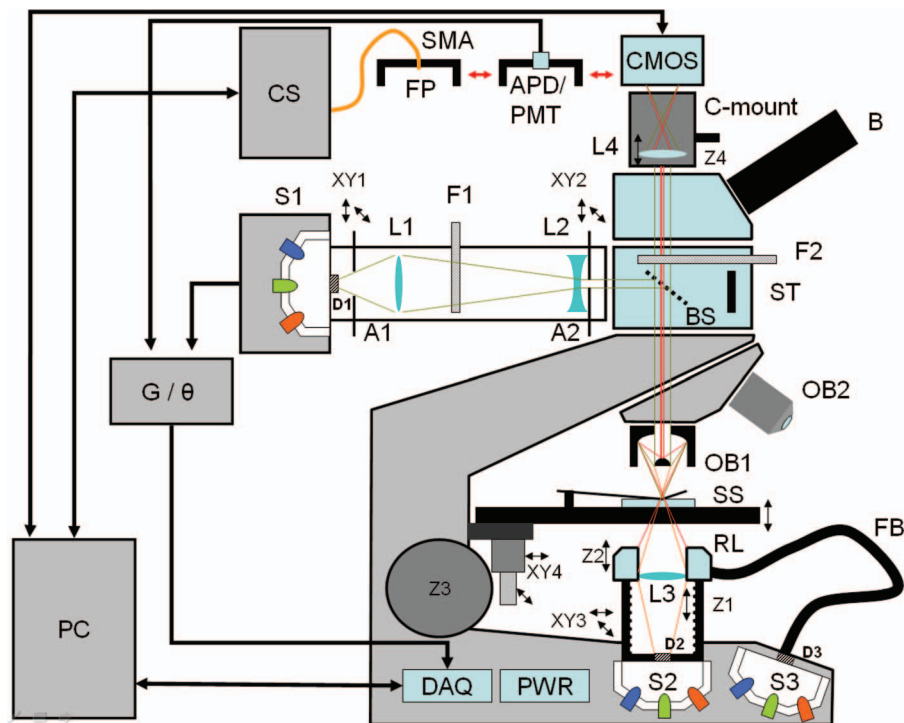
FIG. 1. (Color online) System overview. Three optical multiplexers, S1–S3, provide multispectral illumination from the UV to NIR region in reflectance, transmittance, and scattering mode, respectively. The light from the sample mounted on the sample stage, SS, is collected through a reflective objective OB1. Detection is generally performed by a monochromatic CMOS industrial camera. Alternatively, light can be detected by a compact fiber spectrometer, CS, e.g., for band calibration. Photodiodes or an APD can be used to study fast phenomena. Filter slots F1 and F2 can be used for various filters in polarization or fluorescence studies.

can be used to measure diffuse and specular reflectance, transmission, absorption, scattering, anisotropic scattering, and excitation-emission matrix fluorescence in 13 spectral bands ranging from 375 to 940 nm. Further, the instrument provides quantitative information on the consistency and spatial variation of the properties within the sample by use of a 5 megapixel CMOS camera.

II. INSTRUMENT AND SYSTEM CONFIGURATION

A. Optics

The instrument is based on a modified metallurgical microscope[23–25] (Brunel Microscopes Ltd. Model, SP80). The original filament light source for reflective imaging was removed. Three of the original lenses and achromats (OL1, OL2, and OL3) were removed, and three new LED multiplexing modules, S1, S2, and S3, were installed, two of them under the sample stage (SS). The modified microscope is shown schematically in Fig. 1.

The light sources, the LED multiplexing modules, are cylindrically symmetric cavities made of highly reflective white teflon, and serve to combine the rays from each LED.[26] For each module (S1, S2, and S3), the optical axes of each LED meet at a common point, where a 5 mm opal diffuser is located (D1, D2, D3, Edmunds Optics, NT46-162). The white teflon cavity enhances the throughput of the light transmitted through the transmissive opal diffusers. When the LEDs are switched on individually, a Lambertian-like source, which is independent of the incident angles, is achieved on the other

side of the diffusers. The LED multiplexing modules have slots for nine 5 mm LEDs; a central one surrounded by eight in a circle. By selecting one triple-band LED and two dual-band LEDs, a total of 13 spectral bands can be achieved ranging from 375 nm to 940 nm (Fig. 2). The LEDs were obtained from Roithner Laser Technik,[21] with details given in next paragraph. This roughly covers the spectral sensitivity range of CMOS imagers, which is also indicated in the figure. Beam centering (XY1) and collimation (XY2) of S1 are achieved by the adjustable apertures A1 and A2, and by the quartz lenses L1 and L2. Dispersive optical components in the instrument are made of quartz to reduce achromatic aberration and lens fluorescence in the illumination profiles towards the UV. Filter slot F1 enables polarizing or low-pass filters to be used for clean-up during fluorescence excitation of the light from S1. The beam from S1 is reflected to the interchangeable objectives OB1, OB2 by a broadband beam splitter. The direct transmission of the light from S1 is terminated on a black, non-fluorescent beam stop, ST. The beam divergence from S2 can be controlled by displacing the lens L3 (Edmund Optics, NT49-959) at the translation stage, Z1. Based on the setting of Z1, the lens L3 images the opal diffuser, D2, either on the sample or on the back of the secondary mirror of the Cassegrainian objective employed, OB1. The setting of Z1 therefore determines whether S2 produces light for scattering or transmission measurements. The light from S3 is fed into a fiber bundle and delivered to a ring light (RL) source (Edmund Optics, NT54-176), which illuminates the sample, at SS, symmetrically, but off-axis. In contrast, S1 and S2 illuminate SS on-axis. Centering of S2 and S3 is achieved using
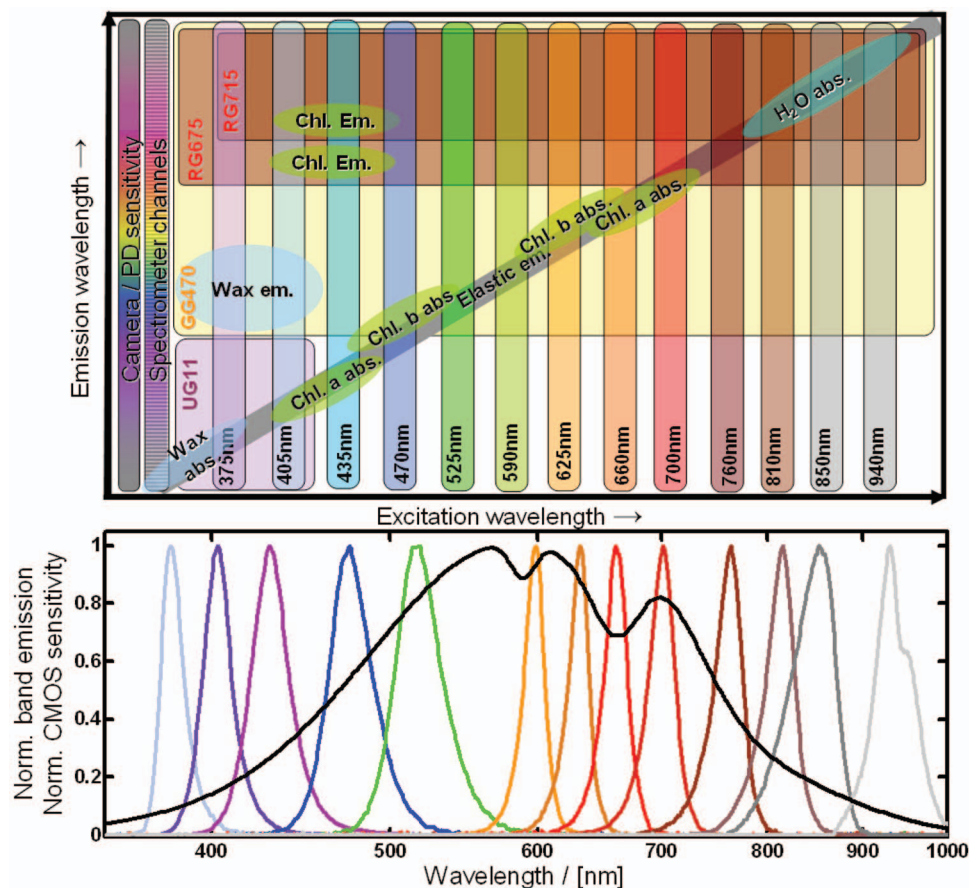
FIG. 2. (Color online) Upper panel: schematic spectral overview of the excitation emission matrix (EEM) with common botanical chromophores. Lower panel: Wavelength of LED emissions and the CMOS camera sensitivity (black curve).

the translation stage XY3. The incident angles from S3 on the sample can be tuned independently by the Z2 translation. In summary, S1–S3 provides monochromatic excitation illumination from the UV to near infrared (NIR) range, from three different angular lobes with respect to the observation lobe. Optical lobes in the instrument operating in different modes are shown in Fig. 3 and will be discussed below.

Particles exhibiting Mie scattering are known to scatter in a complicated angular pattern, which is not resolved by only three angular sectors/lobes. However, angular scans can be performed by translating at Z2, Fig. 1. Also, Mie scattering typically dominates for larger particle sizes in relation to the wavelength which are already spatially resolved by the imager. For smaller particles not spatially resolved, the angular distribution of Rayleigh scattering and emissions after multiple scattering events are considerably less structured, suggesting that a tri-modal measuring strategy is sufficient to describe the scattered distribution. Additional information regarding the number of scattering event can be gained by evaluating the degree of depolarization.

The objectives are either made of transmissive quartz, with low dispersion and long working distance (OB2), or have a Schmidt–Cassegrainian reflective design (OB1; Edmunds Optics, NT58-421) with zero chromatic aberration, numerical aperture NA = 0.28, focal length FL = 13.3 mm, and working distance WD = 23.75 mm. While traditional dispersive objectives provide a single on-axis angular sensitivity lobe, the reflecting objective provides a bimodal, off-axis, and angular sensitivity lobe (Fig. 3). The resulting light from the sample, SS, is projected onto the angularly sensitive lobes and is collimated and propagated back through the beam splitter (BS). The light emitted from the sample passes the second filter slot, F2, where a polarizing filter can be inserted for studies of structural colors, or long-pass filters can be inserted to acquire the inelastic fluorescent elements of the excitation emission matrix (EEM). A full EEM showing the location of important botanical chromophores and the overlap with the instrument bands is presented in Fig. 2. A flip-in prism, P, enables the image to be seen in the visible bands through binoculars B; this facilitates sample adjustment and focusing. The emitted light is imaged directly on the CMOS imaging chip by the reflecting objective, OB1 (Fig. 1). The magnification is determined by the choice of objective and the adjustable distances Z3 and Z4. The camera in a 12 bit industrial class CMOS camera, 5 megapixels (Guppy-503B, Allied Vision Technology, with a MT9P031 sensor from Micron/Aptina). Additional adaptors enable a fiber probe, FB, connected to a compact spectrometer to be used instead of the imaging chip. This can be used for instrument calibration, for studies of detailed spectral features, and for the acquisition of detailed multi-wavelength-excitation fluorescence spectra. Alternatively, the detector can be replaced by a fast avalanche diode (APD) or a photomultiplier tube to record fast photokinetics and fluorescence lifetimes in the frequency domain. In this case, the current of the
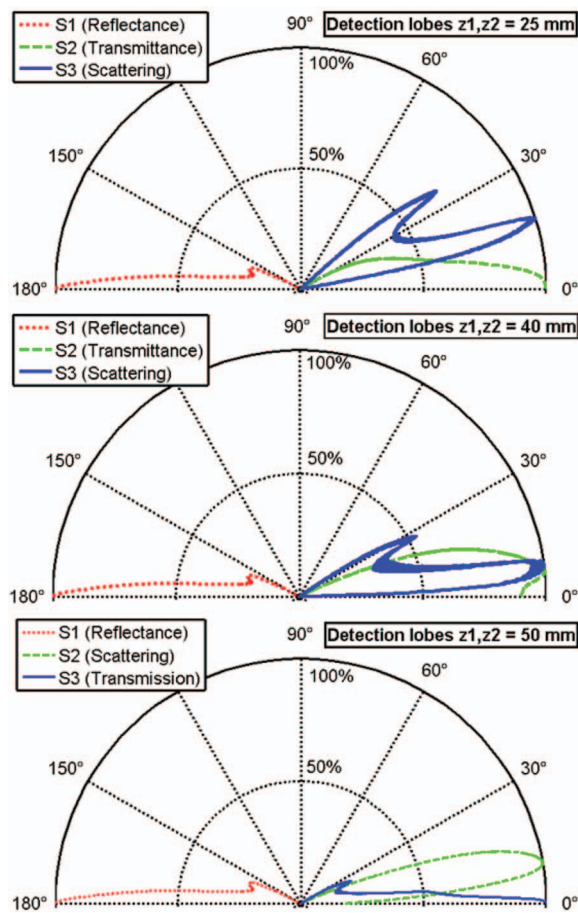
FIG. 3. (Color online) Angular discrimination for three settings of the sub-illumination translation stage (Z1 and Z2 in Fig. 1). Lobes are calculated using ray-tracing methods. The reflectance lobe from S1 remains constant, whereas S3 provides scattering and S2 provides transmittance for high settings/values of Z1 and Z2. When the sub-illumination stage is lowered, light from the opal diffuser, D2, is imaged on the back of the secondary mirror of OB1, and light from the ring light enters the aperture directly. Thus, in this setting S2 provides scattering and S3 provides transmittance.

chosen source is swept over a range of radio frequencies, and the resulting demodulation and phase shifts are detected and recorded at low-frequencies (using, e.g., an AD8302 phase detector, Analog Devices).

B. Electronics

The electronic circuit is controlled by a USB data acquisition board (DAQ, National Instruments, NI USB-6009) and enables multiplexing between different angular modes and different spectral bands. The LEDs are powered by adjustable constant-current sources (Fig. 4). The maximal currents allowed for the NIR sources are somewhat higher than the max current for the UV sources, because of the thermal limitations of LEDs. Since we have 39 sources, we can operate the LEDs in flash mode at currents exceeding the maximum recommendations for the continuous mode by allowing each source to cool between flashes (including a dark measurement). Being able to use higher power increases the signal-to-noise ratio (SNR). In this mode, the clock signal is provided by the camera used for synchronization. A security shut-off is included (in flash mode) in case the clock signal times out. Apart from

the DAQ controlling the current and the source, analog inputs allow the sources to be characterized in terms of voltage-current (U-I) curves. These curves provide information on the temperature of each source. Another interesting feature not presented in the schematics in Fig. 4 is that the circuit can be modified to reverse the voltage on the LEDs in order to use them as wavelength-selective detectors. This provides the opportunity for full EEM measurements on the samples. Detailed mechanical and circuit board drawings can be obtained from Ref. 27 and from the authors on request.

C. Software

The equipment is controlled by LabVIEW software (National Instruments, NI). The user interface is shown in Fig. 5. The program controls camera exposure and gain, LED multiplexing and the current through the NI data acquisition board, DAQ. The graphical interface is constructed around a live preview picture from the camera for easy localization and focusing. Sliders are used to adjust the gain, exposure, and LED currents, while drop down menus are used to select the wavelength band and the angular mode, i.e., reflectance, transmission, or scattering. A live histogram enables the operator to adjust the settings to avoid saturation of the dynamic range. When the settings for a mode and a band have been chosen, they are added to a row in a measurement protocol. The columns of the table are: angular mode, wavelength, LED current, camera gain, exposure, pause between executing each row. Each row corresponds to the acquisition of one monochromatic image. When the whole protocol is executed, the program saves the images on the hard drive together with a copy of the measurement protocol.

Image analysis is performed in MATLAB (Mathworks), where the images are imported and arranged in multidimensional tensors. Calibration and filtering is pursued and analysis is performed according to the need of the studies.

III. SYSTEM CHARACTERISTICS

A. Optical discretization and calibration

As in any modern optical diagnostic method, the light properties are handled numerically by computers and therefore quantized, or otherwise expressed, discretized. The system can be characterized according to the domains listed in Table I.

Some experiments may require the discretization of polarization, inelastic effects such as fluorescence, or phase in interferometric setups. Below we will describe and characterize the multispectral microscope in the five domains listed above.

B. Dynamic domain calibration and light intensity

In general, a multidimensional matrix or tensor, U, is obtained, containing matrix elements of intensity counts, u. By comparing the intensity counts before, U_0, and after interaction with a sample U_{sample}, a number of optical properties of the sample can be determined, and analyzed along each
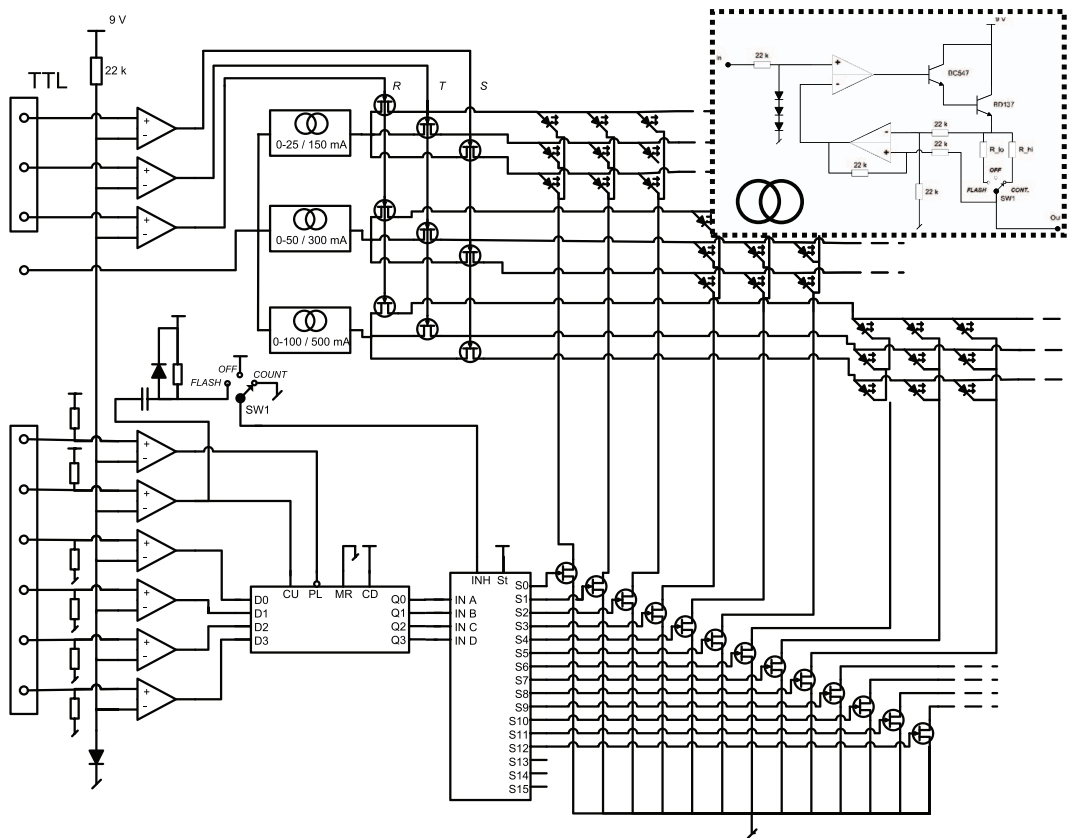
FIG. 4. Electronic schematic used for the multiplexing of sources. Inset: electronic scheme for the adjustable constant-current driver. UV and blue LEDs are driven with currents up to 25 mA, whereas the NIR LEDs can be driven with up to 100 mA.

domain. The dark tensor, U_{dark}, i.e., the contribution arising from the background and dark current in the detector, is subtracted from both these measurements. Since dark current varies with electronic gain, exposure time and instrument temperature, the measurement protocols for U_{dark}, U_0, and U_{sample} should be identical. After dark current subtraction each element in the sample tensor is divided by the corresponding element in a bright reference image. This operation cancels out different emissive yields of the LEDs, electronic gains, and exposures for each band, and also the variation in the illumination intensity over the field of view (FOV):

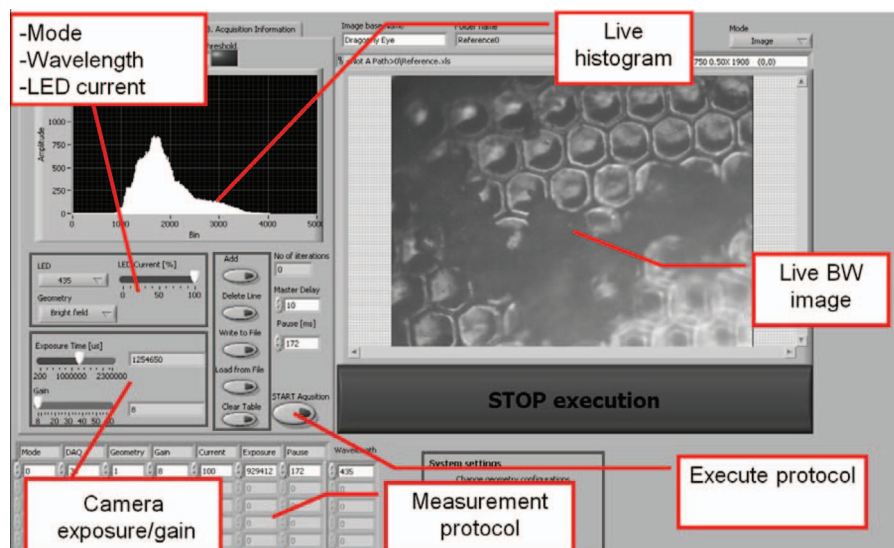$$\{T, R, S\} = \frac{U_{sample} - U_{dark}}{U_0 - U_{dark}}, \tag{1}$$

FIG. 5. (Color online) Graphical user interface (GUI) for controlling the LabView software. The GUI includes a live monochrome preview, live histogram, and settings can be made for the LEDs and camera. The settings can be added to a measurement protocol, which can then be executed automatically.

TABLE I. Discretization of different optical processes.

Subject to discretization	Light intensity	Spatial origin	Time	Light energy	Propagation
Domain	Dynamic	Spatial	Temporal	Spectral	Angular
Discretized by	Bits	Pixels	Frames	Spectral bands	Scattering lobes
Source constraint	Number of photons	Illumination beam profile	Exposure gate	Spectral linewidth	Beam divergence
Detector constraint	QE and SNR	Point spread function	Flash envelope	FWHM band sensitivity	Acceptance angle
Range	Full well and dynamic range	Field of view	Recording time	Spectral coverage	Numerical aperture
Quantity preserving initial condition	Bright reference	Specular, ballistic	Instant	Elastic	Ballistic
Phenomena causing changes in the property	Absorption, scattering	Photo-migration	Fluorescence, migration delay	Fluorescence, Raman, Doppler, harmonics, ionization	Refraction, reflection, Mie and Rayleigh scattering

where T is the transmittance, R is the reflectance, S is the scattering, U_{sample}, is sample tensor, U_{dark} is dark tensor, and U_0 is bright tensor. Details regarding calibration of each mode can be found in Table II.

The optical properties of the sample can be used to improve our fundamental understanding, alternatively T, R, and S can be used in multivariate mathematics, and chemometric methods can predict special features of interest. Such analysis can be useful, e.g., for designing systems with optimal wavelengths for specific diagnostic tasks.

The CMOS imager used, gives rise to so-called "salt and pepper noise," which implies that certain pixels are saturated and certain pixels are entirely black. This type of noise is static and cannot be removed by temporal averaging; instead a spatial 2D median filter removes this noise entirely. This operation decreases the spatial resolution slightly, but the spatial resolution of our system is mainly constrained by the optical resolution, and not by the spatial sampling of pixels.

C. Spatial domain and field of view

In the spatial domain, the image of the object will be convoluted with the point spread function, PSF, well known from Fourier optics theory,

$$u_{pixel} = \int_{-\infty}^{\infty} \int_{-\infty}^{\infty} (E_{profile}(x, y)\text{PSF}_{pixel}(x, y))$$
$$\otimes I(x, y)dxdy, \tag{2}$$

where u_{pixel} is the contribution to the signal intensity in a given pixel, $E_{profile}$ is the illumination profile, I is the intensity from the sample, PSF_{pixel} is the point spread function for a given pixel, and x, y is the spatial coordinates in the object plane.

The spatial confinement can either be provided by a narrow PSF and/or by a narrow scanning illumination profile as in confocal microscopy. As will be shown below, illumination and detection can be freely interchanged mathematically because of the fact that most optical processes are reciprocal and the same result is obtained when source and detector are swapped.[28] Equation (2) assumes a negligible amount of multiple scattering and photo-migration, which to some extent is valid in microscopic samples.

The CMOS imager has pixel sizes of 2.2 μm $\times$ 2.2 μm and an effective chip size of 5.7 mm $\times$ 4.3 mm. The finite reflective objective provides a magnification of 15 times, and thus the FOV is roughly 380 μm $\times$ 286 μm. Each pixel therefore has a square "footprint" of 146 nm $\times$ 146 nm. Other dispersive objectives with magnifications of 4$\times$ and 10$\times$ included with the original microscope provide a larger FOV, of up to one millimeter. The chromatic properties of these objectives are less convenient than for the reflecting objective; further they will themselves contribute a significant amount of reflectance, and thus consume a considerable amount of the dynamic range. Accurate spatial calibration can be achieved by placing objects with known dimensions in the object plane, e.g., micro-rulers.

The SNR in the dynamic domain can be traded off by spatial resolution by spatial averaging[29,30] where especially median filters are effective; see Sec. III B.

TABLE II. Method of calibration for different sensitivity lobes.

Calibration of	Transmission	Reflectance	Scattering
Bright reference, U_0	Plain glass slide	Plain glass slide or opal diffuser	Lambertian opal diffuser
Dark reference, U_{dark}	LEDs off	Empty sample stage	Empty sample stage

D. Temporal domain

Consider the analogous effect of the temporal instrument function,

$$u_{frame} = \int_{0}^{\infty} (E(t)G_{frame}(t)) \otimes F(t)dt, \tag{3}$$

where u_{frame} is the contribution to the signal intensity from a time frame, E is the pulse envelope of illumination, G_{frame} is

the exposure time of the detector, F denotes the changes in the sample over time, and t is time.

Equation (3) states that a fast photograph of a changing process can be achieved either by a short camera exposure, or a short flash of illumination. The assumption made for Eq. (3) to be valid is that the photons should not be delayed by the sample. A delay could be caused by the fluorescence process; however, fluorescence is normally a weak phenomenon compared to elastic phenomena.

For a good SNR, exposure time varies between 0.02 and 2 s, and the acquisition of an entire dataset with 13 bands in transmission, reflection, and scattering typically takes 1 min. The same period is required to obtain the dark and bright references.

As in the spatial domain, the SNR in the dynamic domain can be improved at the expense of the temporal resolution. However, since a large fraction of the noise is static the spatial average is more effective.

E. Spectral range domain

In general in LED spectroscopy it is more convenient to provide more spectral or angular modes by a plurality of LEDs rather than a plurality of detectors,[26,31] because of circuit simplicity and cost. The spectral bands are now defined by the sources rather than by the spectral discrimination on the detecting side (see Fig. 2). The result is equivalent, as is evident from Eq. (4), as long as there is no fluorescence:

$$u_{band} = \int_0^\infty E_{band}(\lambda) D(\lambda) O(\lambda) d\lambda, \qquad (4)$$

where u_{band} is the contribution to the signal intensity from a given spectral band, E is the emission spectrum of the illumination, D is the detector sensitivity spectrum, O is the spectral property of the sample, and λ is the wavelength.

A C-mount to SMA adapter was used to connect the instrument to a fiber (see CS, SMA, FP, in Fig. 1) in order to characterize the system bands with a compact spectrometer (USB2000, Ocean Optics). The effective center wavelength, $\lambda_{band\ center}$, of a spectral band is given by the center of mass formula

$$\lambda_{band\ center} = \frac{\int_0^\infty (V_{band}(\lambda) - V_{dark}(\lambda)) D_{imager}(\lambda) \lambda d\lambda}{\int_0^\infty (V_{band}(\lambda) - V_{dark}(\lambda)) D_{spectrometer}(\lambda) d\lambda}, \qquad (5)$$

where $\lambda_{band\ center}$ is the effective center wavelength for a given band, V_{band} is the spectrometer recording at the image plane, V_{dark} is the dark spectrum, D_{imager} is the sensitivity spectrum of the imager (from manufacturer's datasheet), and $D_{spectrometer}$ is the spectrometer sensitivity including fiber transmission.

The estimated bandwidth, full width at half maximum (FWHM), was compensated by detector sensitivity in a similar way. The measured characteristics of the LEDs used are given in Table III. Many of the sources are now available with an emissive yield several times higher.

TABLE III. Characteristics of LEDs used in the multispectral microscope.

Substrate	Part no.	λ_{band} (nm)	FWHM (nm)	CW max power (mW)
AlGaP	NS375L_ERLM	380	12	26
AlGaP	LED405-33V	405	16	15
AlGaInP	LED435-12-30	430	23	20
InGaN	B5-4RGB-CBA	480	29	20
InGaN	B5-4RGB-CBA	525	34	10
AlGaInP	Y5CA5111P	600	17	55
AlGaInP	B5-4RGB-CBA	630	18	5
AlGaAs	LED660-850-04A	660	22	5
AlGaAs	ELD-700-524	700	25	10
AlGaAs	LED760-940-04A	760	29	15
AlGaAs	ELD-810-525	810	32	28
AlGaAs	LED660-850-04A	850	52	7
GaAs	LED760-940-04A	935	48	14

F. Discretization of light propagation and estimation of angular sensitivity lobes

Several microscopic diagnostic methods are known, such as bright field microscopy, where transmitted light is observed from a thin sample slice; reflection (metallurgical) microscopy, where reflected light from opaque minerals or metallic parts is observed, and dark field microscopy in which the ballistic (non-scattered) light never reaches the detector, and only light scattered into the acceptance angle of the objective is detected. The last mentioned mode greatly enhances contrast in transparent biological samples, where organelles such as nuclei, cell membranes, and mitochondria show increased scattering. Since single scattering is most frequently observed in microscopic samples, the scattering distribution can be expected to have a strong dependence on wavelength, polarization, and size of the scatterer. The three well-known earlier mentioned methods in microscopy can all be summarized to a single consideration regarding the light propagation from the sample in respect to the prior incident propagation. For a given system we can consider a sensitivity lobe as being the spherical convolution between the acceptance of the objective and the angular distribution of illumination impinging on the FOV (See Fig. 3). If the sensitivity lobe covers the scattering angles, θ, close to 0 the system can be used for transmittance measurements, which will be largely influenced by the absorption of the sample according to the Beer–Lambert law. A narrow lobe at $\theta = 0$ implies collimated transmission, whereas a broad lobe implies a diffuse total transmittance measurement. If the system sensitivity lobe instead covers the scattering angles, θ, close to 180°, the system will measure reflectance or backscattering. Such measurements will be greatly influenced by the refractive index of the sample, according to Fresnel's equations. A narrow sensitivity lobe at $\theta = 180°$ often implies a measurement of specular reflectance, whereas a broad lobe would imply a diffuse total reflectance measurement. Alternatively, diffuse reflectance can be measured by observing the depolarized backscatter with crossed polarizers. When the system sensitivity lobe covers θ between 0 and 180°, we refer to a scattering measurement. The contribution here is described by Rayleigh and

Mie scattering theory. Any measurement involving a sample slide will suffer from a constraint inhibiting any effective system sensitivity lobe close to 90° in respect to the normal. Generally, the contribution to a lobe can be thought of as

$$u_{lobe} = \int_{0°}^{180°} \int_{0°}^{360°} (E_{\mathrm{mod}\,e}(\theta, \phi) \otimes D(\theta, \phi)) \, S(\theta) \sin(\theta) d\phi d\theta,$$

$$(6)$$

where u_{lobe} is the contribution to signal intensity falling into a certain lobe, E is the angular distribution of incident illumination for a given mode, S is the scattering distribution of the sample, D is the detection lobe, fixed for the choice of objective, θ is the relative scattering angle perpendicular to object plane, and φ, is the relative scattering angle in object plane.

We note that although both illumination and acceptance lobes are cylindrically symmetric, and although the sample is non-ordered, the scattering angle projection on the object plane, φ, is necessary for the 2D spherical convolution. The resulting effective system sensitivity lobes are still cylindrical and can be presented in a polar plot.

In an ideal case, the sensitivity lobes add up to a unit sphere. In practice, this is generally not achievable. From conservation of energy the following constraint for elastic light is obtained:

$$T + R + S + A \leq 1,$$

$$(7)$$

T, R, and S have been defined above, and A is the absorbance. Several approaches to derive basic optical properties such as the absorption coefficient, $\mu_{\mathrm{abs}}(\lambda)$, the scattering coefficient, $\mu_{\mathrm{scat}}(\lambda)$, anisotropic scattering, g, and refractive index, n, from a vector of contributions to several sensitivity lobes have been successfully applied.[11] Generally, the number of lobes should be at least as many as the number of unknown properties for such an inversion to work. Defining the sensitivity lobes of the instrument is essential as a first step towards quantitative dark-field microscopy, a topic which is currently untouched in general.

By translation of the sub illumination (Z1 together with Z2 in Fig. 1), several angular sensitivity lobes can be obtained with the system presented here. In the upper-most figure in Fig. 3 the optical multiplexer S2 in Fig. 1 accounts for the transmittance measurement, and S3 accounts for the scattering measurement. In the lower-most figure with a different translation of the sub illumination S2 accounts for the scattering, whereas S3 accounts for the transmittance measurement. The lobes in Fig. 3 are obtained by ray-tracing methodology using the FRED (Photon Engineering LLC) software package. The lobes are calculated using the reciprocity of optics, in which we can let the CMOS detector chip be acting as a light source in the ray-tracing simulation. By calculating the 2D convolution between the distribution of angular propagation on the FOV, from both the real light sources and from the imaginary rays from the detector source, we obtain the effective system sensitivity lobes. The lobes in Fig. 3 are cross-sections of the cylindrically symmetric lobes from the convolution. As in Fig. 2 each lobe was normalized to 100% responsivity.
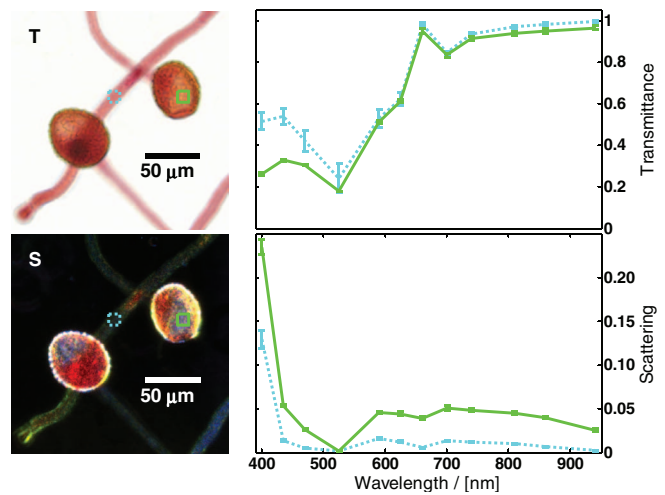

FIG. 6. (Color online) Microspectroscopy of pollen. The upper figures show transmittance, and the lower figures scattering. Proteins and waxes cause differential absorption in the blue and UV regions.

IV. EXAMPLES OF AERAS OF APPLICATION

A. Ground truth and bio-aerosol analysis for remote sensing and environmental monitoring

In the area of environmental monitoring and remote sensing, techniques such as light detection and ranging (LIDAR) and hyper-spectral imaging,[2,32–37] have proven efficient in analyzing various types of vegetation, atmospheric gases, and bio-aerosols.[38–40] The methods are known to be especially useful in combination with ground truth measurements, where the basic optical properties of the species of interest are investigated.[41] In Fig. 6, two pollen germinations were placed in the FOV. The picture to the upper left shows true color RGB (630 nm, 525 nm, 470 nm) transmission. The pollen tube seen as a pink fiber-like structure measures just 10 μm in diameter. The pollen grain is considerably larger and appears as a sphere. In the lower left picture the same situation is shown in scattering imaging where the glass slide appears black. Two regions of interest (ROIs) were selected, one for the pollen tube and one for the pollen grain. The corresponding spectra are presented on the right. The error bars represent the variance within the ROIs. The pollen grain shows higher absorption in the violet region than the tube. The pollen grain is known to contain waxes and proteins which protect the genetic material. In scattering mode, the tubes appear mostly clear and transparent, whereas the grains have increased scattering and light is multiply scattered (whitish) due to the fractal elements of the grain. The spectral difference could provide a method for remote estimation of the grain/tube ratio useful in bio-aerosol measurements by differential absorption LIDAR (DIAL).[39]

Polarization analysis is a useful tool to investigate the spectral signatures of bio-aerosols. Two damselfly abdomens, one of each gender, (dried specimen) were placed in the instrument (Fig. 7). *Caloptoryx splendens* is known to produce bluish and greenish colors by coherent scattering. Such structural colors would appear in the polarized reflectance, whereas they would vanish in the depolarized reflectance.
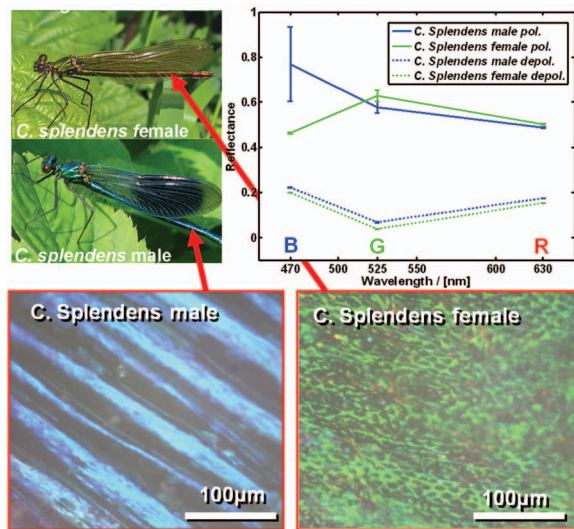
FIG. 7. (Color online) Demonstration of polarization effects in structural colors of a damselfly species. Note that the gender-specific spectral feature disappears in the depolarized reflectance—an inherent property of structural colors.

Spectral features based on differential absorption would be more prominent in depolarized reflectance since the specular part of reflectance would be removed. The RGB values for polarized and depolarized reflectance light were normalized to the polarized and depolarized reflectance from white paper, respectively. The dark reference must also be measured for each kind of polarized light because of the contribution from the beam stop, ST (see Fig. 1). Linear film polarizers (Edmunds Optics, NT45-667) for visible light (450–650 nm) were placed in filter positions F1 and F2. Three pieces of polarizers were cut out from a sheet, two identical and one perpendicular to the polarizing axis of the sheet. Polarization studies over a broader spectral range could be achieved with wire grid polarizers or Glan Thomson polarizers, but with a completely different cost.

Remote monitoring and classification of insects have so far been carried out for diverse purposes such as basic evolutionary ecology,[41] landmine detection,[42] and the evaluation of pest pheromone traps in agriculture.[43] Apart from use in insect studies,[41] the instrument has also been used to obtain supporting data for the remote sensing of birds.[44]

B. Vegetation analysis in agriculture

Several commercial LED-based systems exist and are often used to measure leaf reflectance, transmittance, scattering, and chlorophyll fluorescence. Such measurements are related to the photon migration in forest canopies,[38,45,46] and multispectral satellite imaging is crucial in managing modern agriculture in terms of determining which crops are being grown, and foreseeing catastrophes such as drought or epidemics related to monocultures. The image on the left in Fig. 8 shows a composite image of a Chinese strawberry tree leaf (*Myricaceae Myrica rubra*). The sample has chlorophyll-filled patches with bright veins in between. Near-infrared (810 nm) transmission is shown as red, 810 nm scattering as green, and chlorophyll fluorescence at 700 nm is presented as blue. The fluorescence is induced with the 435 nm LED in reflectance mode and detected through a long-pass filter at 470 nm placed at F2 (See Fig. 1). In principle, multi-wavelength-excitation imaging could be performed without having to remove the long-pass filter.[47] Other parameters related to the condition of the plant can be extracted using photokinetics and the Kautsky process.[48,49] Such temporal characteristics have been used in gender classification for improved crop yield.[50,51] The decay curve on the right in Fig. 8 shows the decay of chlorophyll fluorescence associated with the entire image. In principle, a lifetime image could be generated, in which each pixel is color-coded according to the decay time; however, in this specimen there was no significant spatial variance of the decay times. The data were fitted to the following model:
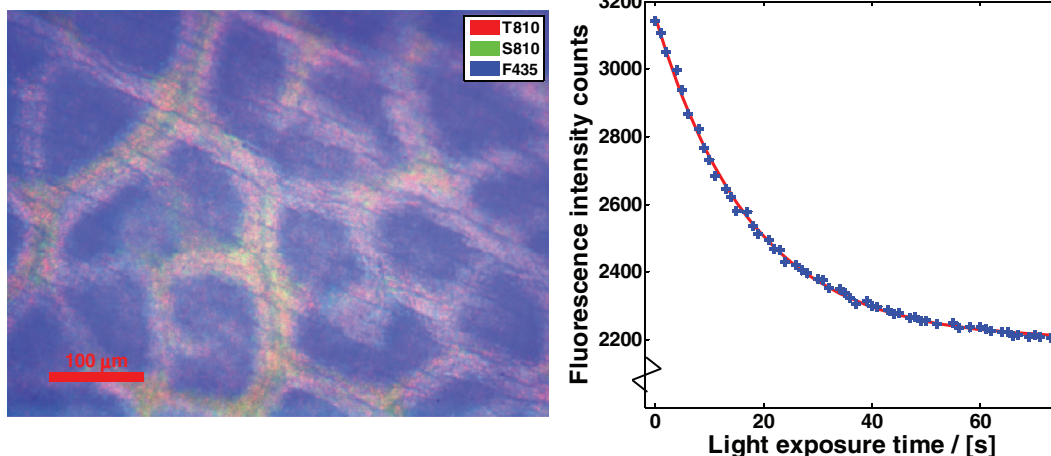
$$F(t) = F_0 e^{-t/\tau} + F_b, \tag{8}$$

FIG. 8. (Color online) Left: composite image of a *Myricaceae Myrica rubra* leaf. The 810 nm transmittance is illustrated in red, the 810 nm scattering in green, and 435 nm-induced chlorophyll fluorescence at 700 nm is illustrated in blue. Right: the photochemical reaction of chlorophyll over time related to the Kautsky processes.
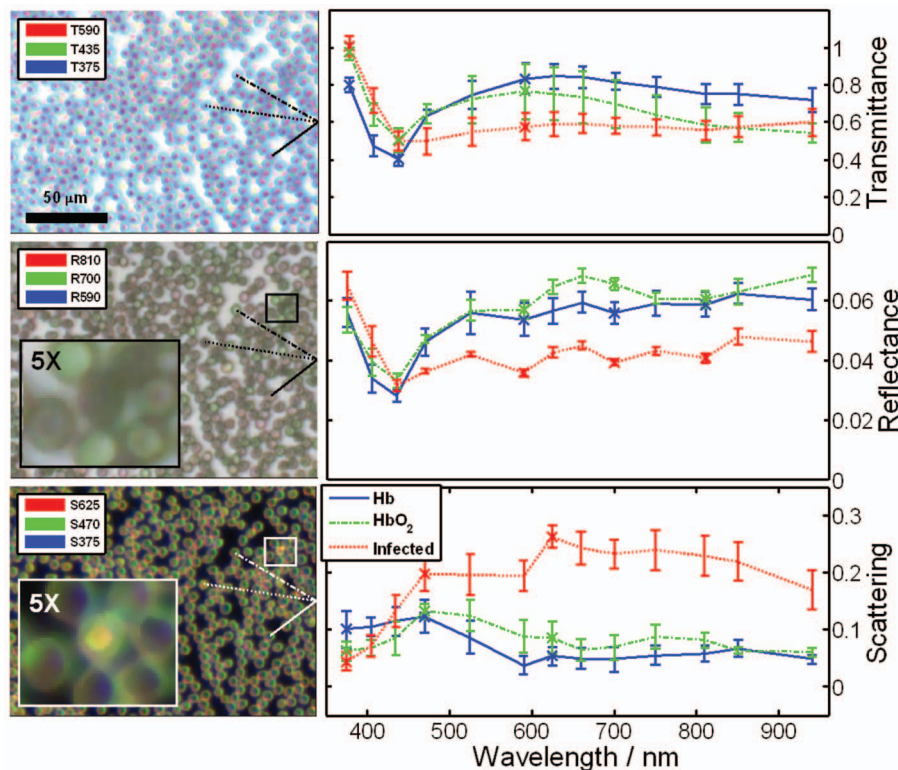
FIG. 9. (Color online) Top left: false color transmittance image of infected blood smear, 590 nm: red, 435 nm: green and 375 nm: blue. Top right: spectra from three ROIs: deoxygenated RBC, oxygenated RBC and a malaria-infected RBC. The error bars indicate within-cell variance. Middle left: false color reflectance image, 810 nm: red, 700 nm: green, 590 nm: blue. The inset shows a 5× zoom. Middle right: corresponding reflectance spectra. Bottom left: false color image of scattering. 625 nm: red, 470 nm: green, 375 nm: blue. The infected RBCs show increased scattering; see example in the 5× inset. Bottom right: corresponding scattering spectra.

where F denotes the fluorescence intensity counts, F_0 denotes initial fluorescence intensity counts, F_b denotes convergent fluorescence intensity counts, and τ is the time constant.

The intensity fell to $F_b/(F_b + F_0) = 69\%$ of the initial value and the time constant was 17.7 s with the 95% confidence interval 17.2–18.2 s. The specimen was a couple of hours fresh and was studied at room temperature. In general, detailed analysis of photokinetics requires careful calibration of the absolute excitation power impinging on the sample.

C. Malaria analysis in parasitological studies

The characteristics of *Plasmodium falciparum* parasites, causing malaria, are presented in Ref. 52. Detection of the parasites usually involve time-consuming staining, and the result relies to a great extent on the experience of the evaluating pathologist.[27,53,54] The delay in diagnosis often means that the patient does not return for care, while an inexperienced evaluator often results in a higher false-negative ratio. The scattering of light from single red blood cells (RBCs) or erythrocytes is described in[55,56]. One alternative to staining and manual evaluation is multispectral imaging[27,54] together with multivariate analysis.[57–60] Fig. 9 shows the results of analyzing a malaria infected blood smear in the instrument. The images are all filtered by a 3 × 3 median filter. Different false-color pictures are presented in transmission, reflectance, and scattering mode in the left of the figure. The legend in each image shows which bands are displayed in the RGB image.

Three cells are selected, and their corresponding spectra are shown for each mode on the right. Error bars represent the variance within a ROI of Ø 3 μm. The RBCs are seen as 7 μm diameter discs; the osmotic pressure causes them to either be inflated or donut shaped,[61] which affects the scattering distribution. The two selected healthy cells in Fig. 9 are both swollen RBCs. In the middle picture of Fig. 9 the reflectance shows a clear circle for the inflated RBCs and a circle with a dot in the middle for the donut-shaped RBCs. The absorption properties of hemoglobin change according to whether the RBC carries oxygen or not.[62] This feature is particularly visible in the red-NIR region around 700 nm, and this effect causes certain RBCs to appear green or pink in the false color reflectance image in Fig. 9. Since healthy human RBCs have no internal structure, scattering takes place mostly at the edges. Infected RBCs scatter significantly higher amount of red and NIR light, and they appear as "glowing" yellow cells in Fig. 9 (bottom left). These interesting results suggest that staining free detection could be improved by including spectrally resolved dark field mode microscopy.

The diffraction limit for the reflecting objective imaging at longest spectral band, 940 nm, corresponds to 2 μm resolution. As can be seen in the zoom inserts, the 7 μm RBCs are resolved close to the diffraction limit. The pixel size is, however, ten times smaller. Because of this oversampling the median filter can be applied to remove the salt and pepper noise essentially without any detrimental effect on the spatial resolution.
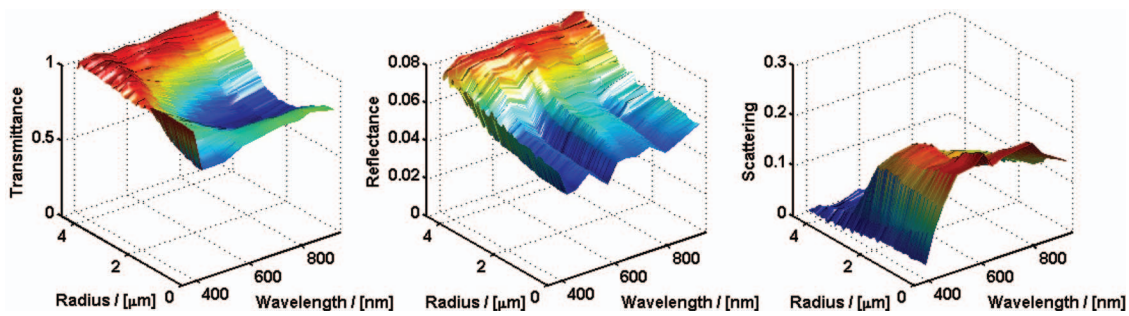
FIG. 10. (Color online) The radial dependence of the transmission, reflectance and scattering spectra from a single healthy red blood cell.

Since RBCs are cylindrically symmetric and align themselves parallel with the microscope slide in a blood smear, the optical properties can be studied as a function of the radius of the cell. Figure 10 shows three such surfaces for transmittance, reflectance, and scattering for a donut-shaped RBC. Healthy RBCs do not scatter red light at the centre due to lack of internal structures. Because of the topology of RBCs, both healthy and infected cells scatter light from the edges. Analysis of the spectral properties in relation to the radius of each cell in the FOV could provide further specificity, for example in healthy RBCs: red light should scatter from the edges but not from the center.

Because of the very large amount of data provided by the instrument, the equipment is especially suited for analyzing variance, both within a cell, between cells and between individuals. Spatial variance can be investigated either as shown above with error bars, or in multivariate analysis, singular value decomposition (SVD), and histograms in one, two, three or more dimensions. All spectra in each spatial pixel in the scenario in Fig. 9 were concatenated (an operation that places transmittance, reflectance, and scattering vectors one after the other). The concatenated vectors were then decomposed by SVD, and from the eigenvalues it could be concluded that most of the variance within the dataset could be explained by just 3 principal spectral components, out of the total of 39 recorded in the 13 bands in 3 angular lobes. Following decomposition, the data are de-concatenated into transmittance, reflectance, and scattering. The weights of the first 3 components are shown in Fig. 11 (left). The new spectral components span up an optimized 3D color space, in which each pixel falls into a given position (see the black dot scatter plot in Fig. 11, right). By counting the number of observations per unit volume it is possible to construct a 3D histogram tensor. Such a 3D histogram is also illustrated in Fig. 11, right, with iso-surfaces encircling three orders of magnitude of count concentrations in the color space. If
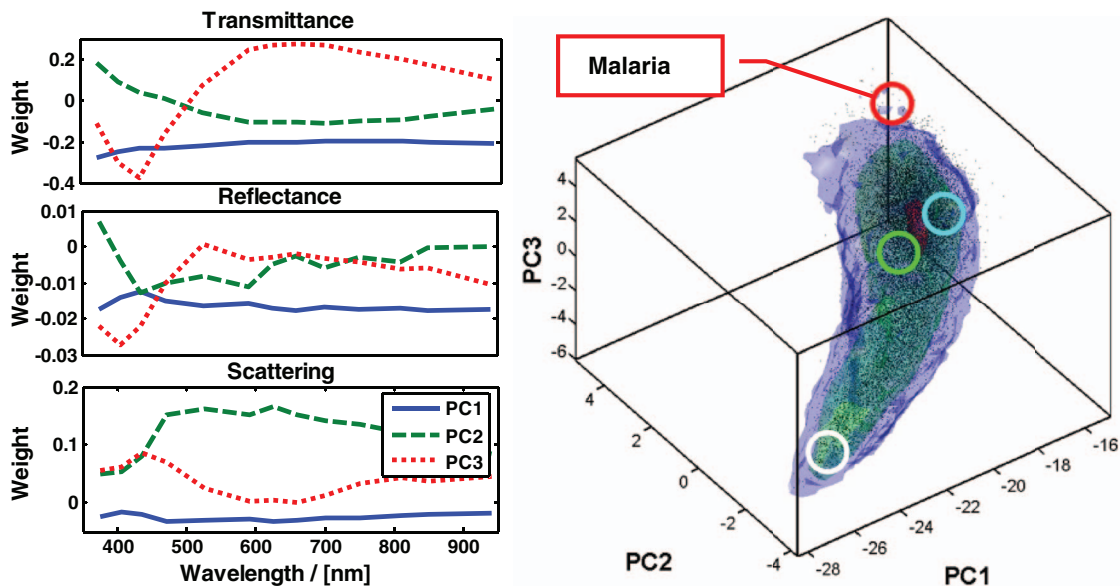

FIG. 11. (Color online) SVD evaluation of infected blood smear. Left: The three components accounting for 75% of the variance in the image. The spectra were concatenated prior to the SVD analysis; thus the components in the various modes are associated. Right: 3D scatter plot with iso-surfaces covering three magnitudes of the 3D probability histogram. The white circle at the bottom indicates the location of the pixels from an empty glass slide. Green and cyan circles in the center indicate the averaged location of the two healthy RBCs from Fig. 9. The core of the scatter plot indicated by a red isosurface, corresponds to the cell peripheries. The infected blood cell illustrated in Fig. 9 falls into the sparse region indicated by the red circle at the top of the figure.

a certain volume unit in the space can be associated with infected RBCs, the counts in that unit volume will relate linearly to the percentage of infected RBCs.

V. COMMENTS ON THE CONSTRUCTION AND UTILIZATION OF THE INSTRUMENT

The powerful yet inexpensive instrument described in this paper is of great interest in many contexts, not least in solving problems in the Developing World. The assembly and testing of replicas of the described instrument was done during a two-week workshop at the Laser and Fiber Optical Centre, LAFOC, University of Cape Coast, UCC, Ghana. A total of nine units were constructed. The cost of materials for each instrument was approximately 5 000 €. The microscopes are now distributed among the participants from six institutes: LAFOC-UCC-Ghana; Laboratory of Instrumentation Image and Spectroscopy, National Polytechnic Institute of Yamoussoukro, Ivory Coast; Nuclear Laboratory, University of Cheikh Anta Diop of Dakar, Senegal; Department of Physics, University of Bamako, Mali; Department of Physics, University of Nairobi, Kenya; and Department of Instrumentation, University of Colombo, Sri Lanka. Contact details can be provided by the authors upon request. A web community has been established for sharing and discussing data and calibration methods, etc. So far short measurement campaigns have been conducted in Ivory Coast, Senegal, Mali, and Sweden.

VI. SUMMARY AND CONCLUSION

We have described the design and calibration of a new general purpose multispectral microscope, capable of acquiring megapixel images of microscopic scenes from the UV to NIR, thus providing millions of transmittance, reflectance, and scattering spectra. We have discussed optical discrimination, and we have briefly described environmental sensing and parasitological applications. We have demonstrated polarization and fluorescence studies, and discussed a number of multivariate methods for data evaluation. In conclusion, the instrument described constitutes a powerful development platform for a multitude of applications. Since the presented instrument is mainly based on an imaging detector, the spatial resolution or optical sectioning does not compare to confocal methods[63] or super resolution methods.[64,65] Instead, the strength of this instrument should be found in the broad spectral range covered, the combination of plurality of angular modes and the cost and simplicity of the construction. The vast majority of other multispectral imagers are based on spectral discrimination on the detection side with considerable photon losses associated. Typically this is achieved by spatial scanning combined with costly diffraction gratings,[63] or more recently, by prism-grating-prism devices.[66] Alternatively, spectral discrimination can be achieved by temporal sequencing, like in the present study, but performed with tunable wavelength filters on the detection side.[67] Spectrally resolved transmission microscopy has previously been pursued commercially by traditional methods.[25] Especially the absorption of organic fibers in the UV has led to various applications in forensic science.

Multispectral fluorescence microscopy was pursued in Ref. 63 also by use of a diffracting spectrometer. Multispectral macro imaging by multiplexing of LEDs has been pursued commercially [31] in the VIS-NIR range; however, only considering reflectance and employing dispersive objectives.

ACKNOWLEDGMENTS

[1] S. Svanberg, *Atomic and Molecular Spectroscopy* (Springer, Heidelberg Berlin 2004).

[2] S. Svanberg, *Multi-spectral Imaging: From Astronomy to Microscopy—From Radiowaves to Gamma Rays* (Springer, Heidelberg Berlin, to be published).

[3] V. Tuchin, *Tissue Optics: Light Scattering Methods and Instruments for Medical Diagnosis*, 2nd ed. (SPIE, Bellingham, 2007).

[4] S. Jacques and B. Pogue, J. Biomed. Opt. **13**, 041302 (2008).

[5] L. G. Henyey and J. L. Greenstein, Astrophys. J. **93**, 70 (1941).

[6] Y. M. Timofeyev and A. V. Vassilev, *Theoretical Fundamentals of Atmospheric Optics* (Cambridge International Science Publishing, Cambridge, UK, 2008).

[7] X. Li, A. H. Strahler, and C. E. Woodcock, IEEE Trans Geosci. Remote Sens. **33**, 466 (1995).

[8] *Handbook of Biomedical Fluorescence*, edited by M. A. Mycek and B. W. Pogue (CRC, New York, 2003).

[9] M. Brydegaard, P. Lundin, Z. Guan, A. Runemark, S. Åkesson, and S. Svanberg, Appl. Opt. **49**, 4531 (2010).

[10] T. J. Bjärang at FOSS Analytical, U. S. patent 7,830,530 B2 (November 9, 2010).

[11] A. M. K. Nilsson, C. Sturesson, D. L. Liu, and S. Andersson-Engels, Appl. Opt. **37**, 1256 (1998).

[12] M. Kim, Y. Chen, S. Kang, I. Kim, A. Lefcourt, and M. Kim, Appl. Spectrosc. **60**, 1210 (2006).

[13] M. Brydegaard, N. Haj-Hosseini, K. Wårdell, and S. Andersson-Engels, IEEE Photon. J. **3**, 407 (2011).

[14] S. Fantini, M. A. Franceschini, J. B. Fishkin, B. Barbieri, and E. Gratton, Appl. Opt. **33**, 5204 (1994).

[15] E. Gratton, S. Fantini, M. A. Franceschini, G. Gratton, and M. Fabiani, Philos. Trans. R. Soc. London, Ser. B **352**, 1354 (1997).

[16] B. Yuan, S. A. Burgess, A. Iranmahboob, M. B. Bouchard, N. Lehrer, C. Bordier, and E. M. C. Hillman, Rev. Sci. Instrum. **80**, 043706 (2009).

[17] E. F. Schubert, *Light-Emitting Diodes*, 2nd ed. (Cambridge University Press, Cambridge, England, 2006), p. 432.

[18] R. W. Cole and J. N. Turner, Microsc. Microanal. **14**, 243 (2008).

[19] P. Herman, B. P. Maliwal, H. J. Lin, and R. Lakowicz, J. Microsc. **203**, 176 (2001).

[20] PicoQuant, 2011; see http://www.picoquant.com.

[21] Roithner LaserTechnik GmbH Austria, 2011; see http://www.roithner-laser.com.

[22] G. C. Holst and T. S. Lomheim *CMOS/CCD Sensors and Camera Systems* (SPIE, Bellingham, 2007), p. 355.

[23] D. B. Murphy, *Fundamentals of Light Microscopy and Electronic Imaging* (Wiley, New York, 2001), p. 360.

[24] F. J. Kao and P. Török, *Optical Imaging and Microscopy: Techniques and Advanced Systems*, 2nd ed. (Springer-Verlag, Berlin, 2007), p. 395.

[25] Craic Technologies ™, 2011; see http://www.microspectra.com .

[26] M. Brydegaard, Z. Guan, and S. Svanberg, Am. J. Phys. **77**, 104 (2009).

[27] A. Merdasa, "Lund Reports on Atomic Physics LRAP-415," M.S. thesis (Atomic Physics Division, Lund University, 2010).

[28] E. Hecht, *Optics*, 4th ed. (Addison-Wesley, Reading, MA, 2002).

[29] R. C. Gonzalez and R. E. Woods, *Digital Image Processing*, 3rd ed. (Pearson Prentice Hall, Upper Saddle River, NJ, 2008).

[30] C. H. Chen, *Image Processing for Remote Sensing* (CRC, Boca Raton, FL, 2008).

[31] Videometer A/S , 2011; see http://www.videometer.com.

[32] S. Svanberg, "LIDAR," in *Handbook of Lasers and Optics*, edited by F. Träger (Springer, Heidelberg, 2007) p. 1031.

[33] D. M. Winker, C. A. Hostetler, M. A. Vaughan, and A. H. Omar, PC-SCI-202.01 (NASA, 2006); see www.calipso.larc.nasa.gov.

[34] A. P. Cracknell and L. W. B. Hayes, *Introduction to Remote Sensing*, 2nd ed. (CRC, Boca Raton, FL, 2007).

[35] M. Borengasser, W. S. Hungate, and R. Watkins, *Hyperspectral Remote Sensing: Principles and Applications* (CRC, Boca Raton, FL, 2008).

[36] A. K. Maini and V. Agrawal, *Satellite Technology: Principles and Applications* (Wiley, Chichester, 2007).

[37] F. M. Mims III, Appl. Opt. **31**, 6965 (1992).

[38] A. Ounis, Z. G. Cerovic, I. Moya, and J. M. Briantais, Remote Sens. Environ. **76**, 33 (2001).

[39] R. Grönlund, M Sjöholm, P. Weibring, H. Edner, and S. Svanberg, Atmos. Environ. **39**, 7474 (2005).

[40] J. R. Simard, G. Roy, P. Mathieu, V. Larochelle, J. McFee, and J. Ho, IEEE Trans Geosci. Remote Sens. **42**, 865 (2004).

[41] Z. G. Guan, M. Brydegaard, P. Lundin, M. Wellenreuther, A. Runemark, E. I. Svensson, and S. Svanberg, Appl. Opt. **49**, 5133 (2010).

[42] D. S. Hoffman, A. R. Nehrir, K. S. Repasky, J. A. Shaw, and J. L. Carlsten, Appl. Opt. **46**, 3007 (2007).

[43] L. Mei, Z. G. Guan, H. J. Zhou, J. Lv, Z. R. Zhu, J. A. Cheng, F. J. Chen, C. Löfstedt, S. Svanberg, and G. Somesfalean, "Agricultural pest monitoring using fluorescence lidar techniques Feasibility study," Appl. Phys. B: Lasers Optics (in press).

[44] P. Lundin, P. Samuelsson, S. Svanberg, A. Runemark, S. Åkesson, and M. Brydegaard, Appl. Opt. **50**, 3396 (2011).

[45] R. Furfaroa and B. D. Ganapola, Transp. Theory Stat. Phys. **36**, 107 (2007).

[46] FORCE, A real-time optical solutions for sustainable agriculture, FORCE-A, Multiplex®2, 2007); see www.force-a.eu.

[47] S. J. Hart and R. D. Jiji, Analyst (Amsterdam) **127**, 1693 (2002).

[48] J. R. Lakowicz, *Principles of Fluorescence Spectroscopy*, 3rd ed. (Springer, Heidelberg, 2006), p. 725.

[49] G. Agati, Pure Appl. Opt. **7**, 797 (1998).

[50] S. Ek, B. Anderson, and S. Svanberg, Spectrochim. Acta, Part B **63**, 349 (2008).

[51] B. Anderson, P. K. Buah-Bassuah, and J. P. Tetteh, *Winter College on Optics and Energy, International Centre for Theoretical Physics (ICTP)*, Trieste, Italy, 2010.

[52] *Malaria: Drugs, Disease and Post-genomic Biology*, edited by D. Sullivan and S. Krishna (Springer, Heidelberg, 2010), p. 444.

[53] World Health Organization, *Basic Malaria Microscopy Part I. Learner's Guide*, 2nd ed. (WHO Press, Geneva, Switzerland, 2010), p. 80.

[54] J. T. Zoueu, G. L. Loum, T. C. Haba, M. Brydegaard, and H. Menan, J. Appl. Sci. **8**, 2711 (2008).

[55] M. Hammer, D. Schweitzer, B. Michel, E. Thamm, and A. Kolb, Appl. Opt. **37**, 7410 (1998).

[56] A. M. K. Nilsson, P. Alsholm, A. Karlsson, and S. Andersson-Engels, Appl. Opt. **37**, 2735 (1998).

[57] T. W. Anderson, *An Introduction to Multivariate Statistical Analysis*, 3rd ed. (Wiley, Hoboken, NJ, 2003).

[58] A. C. Rechner, *Methods of Multivariate Analysis* (Wiley, New York, 2002).

[59] K. R. Beebe and B. R. Kowalski, Anal. Chem. **59**, 1007A (1987).

[60] P. Weibring, T. Johansson, H. Edner, S. Svanberg, B. Sundnér, V. Raimondi, G. Cecchi, and L. Pantani, Appl. Opt. **40**, 6111 (2001); P. Weibring, T. Johansson, H. Edner, S. Svanberg, B. Sundnér, V. Raimondi, G. Cecchi, and L. Pantani, *ibid.* **41**, 434 (2002).

[61] Y. Tan, D. Sun, J. Wang, and W. Huang, IEEE Trans. Biomed. Eng. **57**, 1816 (2010).

[62] D. J. Faber, M. C. G. Aalders, E. G. Mik, B. A. Hooper, M. J. C. v. Gemert, and T. G. v. Leeuwen, Phys. Rev. Lett. **93**, 028102 (2004).

[63] M. B. Sinclair, D. M. Haaland, J. A. Timlin, and H. D. T. Jones, Appl. Opt. **45**, 6283 (2006).

[64] S. W. Hell, Nat. Biotechnol. **21**, 1347 (2003).

[65] M. J. Rust, M. Bates, and X. Zhuang, Nat. Methods **3**, 793 (2006).

[66] E. Herrala, J. T. Okkonen, T. S. Hyvarinen, M. Aikio, and J. Lammasniemi, Proc. SPIE **2248**, 33 (1994).

[67] N. Gat, Proc. SPIE **4056**, 50 (2000).